JOURNAL OF AIRCRAFT
Vol. 37, No. 2, March–April 2000

Heat and Mass Transfer in the Case of Anti-Icing System Simulation

François Morency*
École Polytechnique de Montréal, Montréal, Québec H3C 3A7, Canada
Fatih Tezok†
Bombardier Aerospace, Dorval, Québec H4S 1Y9, Canada
and
Ion Paraschivoiu‡
École Polytechnique de Montréal, Montréal, Québec H3C 3A7, Canada

Aircraft manufacturers need anti-icing system simulations to help in the design of ice protection systems. Heat and mass transfer predictions obtained with two different methods to solve the boundary layer in the case of an anti-icing simulation are compared. The integral method and the finite difference method are used to solve the boundary-layer equations, including the mass diffusion equation. The boundary-layer solvers are implemented into the code CANICE, which models the ice accretion process. Comparison of heat and mass transfer distributions and surface temperature distributions are made. Surface temperatures predicted with the finite difference method are closer to experimental results than surface temperatures predicted with the integral method.

Nomenclature

c	= airfoil chord, m
c_p	= specific heat of air, 1004.76 J/(kg K)
c_w	= specific heat of water, 4218 J/(kg K)
F	= shear force on water film, N/m^2
f	= fraction of water that freezes, $\dot{m}_{gl}/\dot{m}_{\text{tot}}$
H	= total enthalpy, J/kg
$\dot{H}$	= mass flow of enthalpy, J/s
h_x	= heat transfer coefficient, W/(m^2 K)
k	= thermal conductivity, W/(mK)
L_e	= latent heat of evaporation, 2512.08 kJ/kg
L_f	= latent heat of fusion, 334.944 kJ/kg
$\mathcal{M}$	= molecular mass, kg/kmol
$\dot{m}$	= mass flow rate, kg/s
$\dot{m}''$	= mass flow rate per unit area, kg/m^2 s
m_j	= mass fraction of substance j
$(\dot{m}_j)''_s$	= evaporation rate, kg/m^2 s
P	= pressure, N/m^2
P_v	= partial vapor pressure of water, N/m^2
Pr	= Prandtl number, $\mu c_p/k$
Q	= heat, W
Q''	= heat flux, W/m^2
Q_{bl}	= heat lost by convection, W
R_x	= $u_e x/\nu$, Reynolds number
Sc	= Schmidt number
s	= curvilinear distance from stagnation point, m
T	= temperature, K
T_b	= bulk temperature in the water film, K
u, v	= velocity component, m/s
u_τ	= $\sqrt{(\tau/\rho)}$ friction velocity, m/s
v_w	= transpiration velocity, m/s
x, y	= spatial coordinate, m
β	= collection efficiency
γ_j	= mass diffusion coefficient, kg/(ms)
δ	= water film thickness, m
δl	= boundary-layer thickness, m
ε_m	= eddy viscosity, m^2/s
μ	= dynamic viscosity, Ns/m^2
ν	= kinematic viscosity, m^2/s
ρ	= density, kg/m^3
τ	= shear stress at the wall, N/m^2

Subscripts

air	= property of air
bl	= boundary layer
e	= evaluated at the edge of the boundary layer
gl	= ice
imp	= relative to the water caught by airfoil
in	= entering a control volume
out	= leaving a control volume
s	= evaluated at y equal to 0 in the boundary layer
t	= turbulent
vap	= vapor
w	= property of water
wall	= in the solid region
∞	= freestream condition

Introduction

FLIGHT safety of aircraft operating under natural icing conditions is one of the major concerns of certification authorities and aircraft manufacturers. Two kinds of in-flight ice protection systems can be used to prevent ice accretion on critical surfaces, such as wings: de-icing or anti-icing systems. The de-icing systems work periodically, waiting for some small amount of ice to accrete before removing it. The anti-icing systems are designed to allow no ice accretion at all, working continuously from the start of any ice accretion event.[1]

Usually, anti-icing systems use heat to keep the cold water caught by the aircraft above the freezing point. This heat comes either from electrical pads installed in the metal skin or from hot air circulating on the inner side of the metal skin. In the case of wings, anti-icing systems are installed in the leading-edge area where water droplets impinge. Although it is possible to keep the leading-edge area just above the freezing point so that water freezes farther downstream,[2]

Presented as Paper 99-0623 at the AIAA 37th Aerospace Sciences Meeting, Reno, NV, 11–14 January 1999; received 21 June 1999; revision received 25 October 1999; accepted for publication 30 October 1999.

*Ph.D. Student, Département de Génie Mécanique, CP 6079, Succ. Centre Ville. Student Member AIAA.
†Staff Specialist, Advanced Aerodynamics, 400 Côte-Vertue.
‡Bombardier Aeronautical Chair Professor, Département de Génie Mécanique, CP 6079, Succ. Centre Ville. Associate Fellow AIAA.

most of the anti-icing systems are designed to evaporate a large part of the water caught by wings.

Aircraft manufacturers use ice accretion simulation codes to help in the design of ice protection systems. Bombardier Aerospace uses the CANICE code developed at the École Polytechnique de Montréal. In addition to its ice accretion simulation capabilities, the CANICE code can also simulate an anti-icing system. Anti-icing simulation results depend mainly on the heat losses to convection and on the evaporation rates used, once the collection efficiencies are determined. In fact, in the case of an evaporative anti-icing system, more than 70% of the energy is used to evaporate the water.[3,4] The objective of the present work is to compare heat and mass transfer predictions obtained with an integral solution and with a finite difference solution of the two-dimensional boundary-layer equations around an airfoil in icing conditions.

A short review of the models used for heat and mass transfer prediction in the case of anti-icing system simulations is first presented. Then, the mathematical model and the highlights of the numerical method used in CANICE are given. Finally, comparison between numerical results and experiments is made for a NACA 0012 in icing conditions.

Previous Works

Al-Khalil[5] has developed a specific model for an airfoil anti-icing system. The two-dimensional conduction equations are solved by a finite volume method in the airfoil skin, and a runback water model is suggested. Water flows on airfoil as a continuous film flow in the impingement region. The continuous film flow breaks down in rivulets when a minimum critical thickness is attained outside of the impingement region. Heat transfer coefficients between water and external air are obtained either experimentally[4] or by numerical methods.[6] Evaporation rates are obtained from the heat transfer coefficient h_x and the ratio of Prandtl number Pr, and Schmidt number Sc:

$$\dot{m}''_{\text{vap}} = \frac{h_x}{c_p}\left(\frac{Pr}{Sc}\right)^{\frac{2}{3}}_{\text{air}} \frac{\mathcal{M}_w}{\mathcal{M}_{\text{air}}}\left[\frac{P_{v,w} - P_{v,e}}{P_e - P_{v,w}}\right] \tag{1}$$

where $P_{v,w}$ is the saturated vapor pressure at the water film surface and $P_{v,e}$ is the local vapor pressure at the edge of the boundary layer accounting for the local relative humidity.

This kind of relation is the one usually used in codes that model the ice accretion process[7,8] to obtain the mass transfer. Only a few models have been tried to predict heat transfer coefficient in these codes. An integral method for heat transfer over rough surfaces, based on equivalent sand grain roughness, is widely used.[9,10]

Some workers have tried to simulate an anti-icing system with a de-icing simulation code. For example, Henry[11] developed a model that simulates two-dimensional heat transfer with an electrothermal anti-icing/de-icing device. Effect of heating on heat transfer coefficients is considered via a complete boundary-layer calculation. Mass transfer rates are calculated from heat transfer coefficients.

Mathematical Model

Numerical simulation of the anti-icing system using an integral method is done with a version of CANICE code described in a previous work.[3] The highlights of these modifications are described here. Special attention is given to the model used with the finite difference method for the external boundary layer.

The anti-icing system is divided in four regions in the mathematical model: 1) the external flow region, 2) the runback water region, 3) the solid region, and 4) the heating area. These four regions are shown schematically in Fig. 1 for the case of a hot air anti-icing system on a single element airfoil. The CANICE code that models the ice accretion process is modified to include the temperature gradient in the runback water, to model the heat transfer in the wall, and to take into account the heating region. An iterative procedure is used to find the surface temperature distribution and the mass of water evaporated. The mathematical models used for each of the four regions are presented in the following subsections.

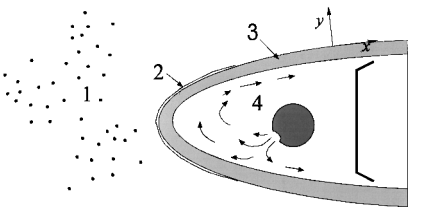

Fig. 1 Typical model of an anti-icing system.

External Flow Region

The external flow region, including airflow around the airfoil and water droplet trajectories, is already modeled in the ice accretion version of CANICE code. First, a potential solution for the flow around airfoil is looked for. Starting upstream of the airfoil, the water droplet trajectories are then found, based on the drag force exerted by the potential velocity field. From the distribution of the droplet impact points, the local collection efficiencies are known and, thus, the mass of water caught by the airfoil. The procedure used has been described in detail by Brahimi et al.[12]

Water on airfoil flows as a thin water film. The shear force, the heat flux, and the evaporation rate at the air–water interface of the film flow are calculated by solving the boundary-layer equations with an integral method or a finite difference method. The continuity equation, the mass diffusion equation, the momentum equation, and the energy equation are as follows, for a two-dimensional boundary layer[13]:

$$\frac{\partial \rho u}{\partial x} + \frac{\partial \rho v}{\partial y} = 0 \tag{2}$$

$$\rho u \frac{\partial m_j}{\partial x} + \rho v \frac{\partial m_j}{\partial y} = \frac{\partial}{\partial y}\left(\gamma_j \frac{\partial m_j}{\partial y}\right) \tag{3}$$

$$\rho u \frac{\partial u}{\partial x} + \rho v \frac{\partial u}{\partial y} = -\frac{\mathrm{d}P}{\mathrm{d}x} + \frac{\partial}{\partial y}\left(\mu \frac{\partial u}{\partial y}\right) \tag{4}$$

$$\rho u \frac{\partial H}{\partial x} + \rho v \frac{\partial H}{\partial y} = \frac{\partial}{\partial y}\left(\frac{k}{c_p}\frac{\partial H}{\partial y}\right) + \mu\left(\frac{\partial u}{\partial y}\right)^2 - u\frac{\mathrm{d}P}{\mathrm{d}x} \tag{5}$$

The mass concentration of substance j in the mixture is given by m_j. For an anti-icing system, only two substances are present: the water and the air. A unit Lewis number assumption, $Le = Pr/Sc = 1$, is made to simplify the energy equation (5). In the case of a turbulent boundary layer, the equations stay the same, except that a turbulent viscosity μ_t, a turbulent mass diffusion coefficient γ_{j_t}, and a turbulent thermal conductivity k_t are added to the laminar ones.

The Cebeci and Smith (see Ref. 14) formulation is used to obtain the eddy viscosity. The eddy-viscosity formula for a flow over a smooth surface with or without heat transfer is defined by

$$(\varepsilon_m)_{\text{in}} = l^2\left|\frac{\partial u}{\partial y}\right|\gamma_{\text{tr}}\gamma \tag{6}$$

for $0 \le y \le y_c$. The value of y_c is defined as the point where $(\varepsilon_m)_{\text{in}} = (\varepsilon_m)_{\text{out}}$. For $y_c < y \le \delta 1$, the eddy-viscosity formula is

$$(\varepsilon_m)_o = 0.0168\left|\int_0^\infty (u_e - u)\,\mathrm{d}y\right|\gamma_{\text{tr}}\gamma \tag{7}$$

The mixing length l is given by

$$l = ky\{1 - \exp[-(y/A)]\} \tag{8}$$

where $k = 0.40$ and A is a damping-length constant, which may be represented by

$$A = 26(\nu/N)u_\tau^{-1} \tag{9}$$

$$N = \left\{(p^+/v_w^+)\left[1 - \exp(11.8v_w^+)\right] + \exp(11.8v_w^+)\right\}^{\frac{1}{2}} \tag{10}$$

$$p^+ = \frac{\nu u_e}{u_\tau^3}\frac{\mathrm{d}u_e}{\mathrm{d}x} \tag{11}$$

$$v_w^+ = v_w/u_\tau \tag{12}$$

An intermittency factor γ_{tr} is used in Eqs. (6) and (7) to represent the transition region from laminar to turbulent flow. It is defined by an empirical correlation,

$$\gamma_{\mathrm{tr}} = 1 - \exp\left[-G(x - x_{\mathrm{tr}})\int_{x_{\mathrm{tr}}}^{x}\frac{\mathrm{d}x}{u_e}\right] \tag{13}$$

where x_{tr} is the location of the start of the transition region. The factor G is evaluated at x_{tr} with

$$G = 8.33 \times 10^{-4}(u_e^3/\nu^2)R_x^{-1.34} \tag{14}$$

Although Eq. (14) has been developed for uncoupled adiabatic flow, it is considered to be a valid approximation for the coupled boundary layer with heat and mass transfer as studied here. The heat and mass transfer rates are relatively small in the case of an anti-icing simulation and have a negligible effect on the momentum boundary layer.

Another factor γ is introduced to account for the intermittency of turbulence as the freestream is approached. It is given by the empirical expression

$$\gamma = \left[1 + 5.5(y/y_0)^6\right]^{-1} \tag{15}$$

with y_0 defined as the y location where $u/u_e = 0.995$.

The turbulent viscosity $\mu_t = \rho\varepsilon_m$, together with the turbulent Prandtl number Pr_t, and the turbulent Schmidt number Sc_t give values for the turbulent conductivity and the turbulent mass diffusion coefficients. A constant value of 0.9 is taken for the turbulent Prandtl and Schmidt numbers.

When an integral method is used, the diffusion equation (3) is not solved. The evaporation rates around airfoil are obtained from the heat transfer coefficients, using an analogy between heat and mass transfer. The equations used to solved the boundary layer by an integral method have already been presented in a previous paper.[3]

At the edge of the boundary layer, the boundary conditions are imposed using the tangential velocity u_e, found from the potential flow solution. For the mass diffusion equation (3), the momentum equation (4), and the energy equation (5), the conditions at $y = \delta 1$ are, respectively,

$$u = u_e \tag{16}$$

$$H = H_e \tag{17}$$

$$m_j = (m_j)_\infty \tag{18}$$

The boundary conditions at the wall, $y = 0$, are slightly more complicated. For the momentum equation (4), that mass enters the boundary layer from the evaporating water film must be taken into account by using a transpiration velocity v_w:

$$u = 0 \tag{19}$$

$$v_w = (\dot{m}_j)_s''/\rho_s \tag{20}$$

For the energy equation (5), the total enthalpy is imposed

$$H_s = c_p T_s \tag{21}$$

The surface temperature used, T_s, is the one at the air–water interface when a water film is present. The water film model presented in the following subsection is used to obtain this surface temperature.

The mass diffusion equation (3) is solved for an imposed mass concentration of water at the wall. The mass concentration of water in air is a function of the partial vapor pressure of water, P_v, and of the local static pressure P_e:

$$(m_j)_{\mathrm{vap}} = P_v/(1.61P_e - 0.61P_v) \tag{22}$$

The partial vapor pressure is a function of the temperature and is given by a polynomial interpolation of the steam table of Ref. 15.

A special case occurs if the evaporation rate is greater than the mass flow rate, $\dot{m}_{\mathrm{in}}'' + \dot{m}_{\mathrm{imp}}''$, in the water film. Then, the evaporation rate must be imposed. This evaporation rate will be less than the one found by imposing the mass concentration of water. The boundary condition becomes, at $y = 0$,

$$m_j = (m_j)_{\mathrm{vap}} \quad \text{if} \quad (\dot{m}_j'')_s \le \dot{m}_{\mathrm{in}}'' + \dot{m}_{\mathrm{imp}}'' \tag{23}$$

$$\frac{\mathrm{d}m_j}{\mathrm{d}y} = \frac{-\dot{m}_{\mathrm{in}}'' - \dot{m}_{\mathrm{imp}}''}{\gamma_j} \quad \text{if} \quad (\dot{m}_j'')_s > \dot{m}_{\mathrm{in}}'' + \dot{m}_{\mathrm{imp}}'' \tag{24}$$

Runback Water Region

Water coming from the droplets that hit the airfoil will freeze, or runback, or evaporate. The runback water is modeled as a continuous film flow with no waves on the airfoil surface, as shown in Fig. 2. In Fig. 2, a film flow of thickness δ is driven by a shear force F and reaches a surface velocity of U_δ. Heat Q_{anti} enters the solid region from the internal hot air. This heat is redistributed before entering the film flow. The incoming heat Q_{wall} is partly used to warm the water film, and the rest, Q_{loss}, is lost by convection and evaporation.

The equation used for the velocity distribution in the water is[3]

$$u_w(x, y) = \frac{1}{2\mu_w}\frac{\mathrm{d}P}{\mathrm{d}x}y^2 + \frac{1}{\mu_w}\left[F - \delta(x)\frac{\mathrm{d}P}{\mathrm{d}x}\right]y \tag{25}$$

The potential velocity field gives the value for the pressure gradient. The film flow is driven by the shear force F applied by the external flow region. The shear force F is the sum of the wall friction τ_{air} exerted by the boundary layer and of the momentum per unit area from incoming water droplets $\dot{m}_{\mathrm{imp}}'' u_{\mathrm{imp}}$:

$$F = \tau_{\mathrm{air}} + \dot{m}_{\mathrm{imp}}'' u_{\mathrm{imp}} \tag{26}$$

The water speed is slow compared to air velocity outside the boundary layer and, thus, can be neglected in the calculation of τ_{air}.

The temperature distribution is approximated by a second-order polynomial:

$$T_w(x, y) = A_T(x)y^2 + B_T(x)y + C_T(x) \tag{27}$$

The bulk temperature in the film flow, T_b, and the heat flux lost to the external airflow, Q_{loss}'', respectively, give the values for coefficients A_T and B_T. The heat flux lost to the airflow includes convection, evaporation, and the energy losses to warm the impinging droplets. The surface temperature of the metal skin sets the C_T value.

Comparison with other numerical results has showed the validity of the model for a very thin film flow.[3]

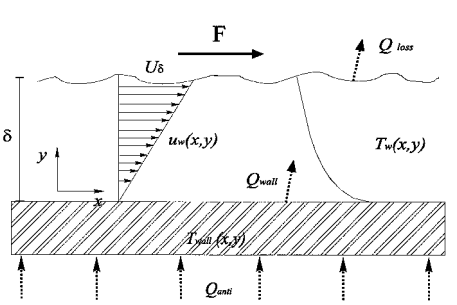

Fig. 2 Runback water model.

Solid Region

The temperature distribution in the metal skin is found by solving the steady two-dimensional conduction equation:

$$\frac{\mathrm{d}}{\mathrm{d}x}\left(k_{\text{wall}}\frac{\mathrm{d}T_{\text{wall}}}{\mathrm{d}x}\right)+\frac{\mathrm{d}}{\mathrm{d}y}\left(k_{\text{wall}}\frac{\mathrm{d}T_{\text{wall}}}{\mathrm{d}y}\right)+S_{\text{wall}}=0 \qquad (28)$$

A source term S_{wall} is included to offer the possibility to simulate electric de-icer pads. When an integral method is used to solve the boundary layer, the temperature is assumed to be constant across thickness, and a one-dimensional formulation of the conduction equation is used.[3]

The boundary condition on the internal side of the metal skin is given either as an imposed heat flux distribution coming from the anti-icing device or as a fixed heat transfer coefficient distribution. On the external side, heat flux is imposed everywhere between the solid surface and the water film or the boundary layer, except when the surface is wet and ice and water are present. In this case, a surface temperature of 0°C is imposed.

Heating Region

The heating area is modeled by a heat flux Q''_{anti}, or by a heat transfer coefficient h_{anti}, or by a source term localized inside the metal skin. When the temperatures are constant across the thickness of the metal skin, in the one-dimensional model case, the y location of the heat source inside the wall has no importance. The heat flux is then considered to come from the internal side of the metal skin, even if the electric de-icer pads are located inside the wall.

Numerical Method

The numerical method used with the integral boundary-layer solution is presented in a previous article.[3] In this section, the implementation in CANICE of a finite difference code and a finite volume code is described.

The panel method of Hess and Smith (see Ref. 16) is first used to obtain the velocity field around the airfoil. Then, each individual droplet trajectory is calculated by integrating the droplet equation of motion with a variable time step Runge–Kutta method of order five.[17] With the droplet impact points on the airfoil, the water mass caught by each panel of the discretized airfoil is found.

Using the compressible version of the Falkner–Skan transformation and the compressible stream function, the coupled boundary-layer equations (3), (4), and (5) are modified. The transformed equations are then solved by a finite difference method using the Box method of Keller (see Ref. 14). This method gives second-order accuracy for arbitrary x and y spacing.

The conduction equation in the solid region is solved by a second-order accurate finite volume method.[18] A quasi-orthogonal grid is used to discretize the airfoil metal skin. Length of the control volumes in the x direction is fixed by the panel sizes used for the solution of the potential velocity field.

The boundary layer is solved for an initial surface temperature, starting at stagnation point. For each panel of the discretized airfoil, the heat exchanged between the metal skin and the water film is calculated. The heat lost by convection to the air and the evaporation rate are first estimated. Then, considering the mass flow rate of water caught, $\dot{m}_{\text{imp}}$, and the mass flow rate in the film flow, $\dot{m}_{\text{in}}$, an energy balance is done on the water film. The energy lost by evaporation is calculated using the evaporation rate and the latent heat of evaporation. The real evaporation rate is given by

$$\dot{m}_{\text{vap}}=\min(\dot{m}_{\text{vap}},\dot{m}_{\text{imp}}+\dot{m}_{\text{in}}) \qquad (29)$$

Four cases can occur on the airfoil surface: 1) no water is present, 2) all of the water freezes, 3) only a fraction of the water freezes, and 4) all of the water is liquid.

The simplest case occurs when no water film is present. Then, heat lost by the wall is equal to heat lost by convection Q_{bl},

$$Q_{\text{wall}}=Q_{bl} \qquad (30)$$

The second case, when all of the water freezes, happens when surface temperature is below 0°C. Then the freezing fraction f is 1, and the ice temperature is equal to the surface temperature.

In the third case, when surface temperature is 0°C, the freezing fraction f is evaluated with

$$f=\frac{\dot{H}_{\text{imp}}+\dot{H}_{\text{in}}+Q_{bl}-Q_{\text{wall}}-\dot{H}_{\text{vap}}-\dot{H}_{\text{tot}}}{\dot{m}_{\text{tot}}L_f} \qquad (31)$$

where $\dot{m}_{\text{tot}}$ represents the amount of water not evaporated,

$$\dot{m}_{\text{tot}}=\dot{m}_{\text{in}}+\dot{m}_{\text{imp}}-\dot{m}_{\text{vap}} \qquad (32)$$

and

$$\dot{H}_{\text{tot}}=\dot{m}_{\text{tot}}c_w T_b \qquad (33)$$

$$\dot{H}_{\text{vap}}=\dot{m}_{\text{vap}}(c_{w,g}T_s+L_e) \qquad (34)$$

In Eq. (34), $c_{w,g}$ is the specific heat of water at the proper state (liquid or ice) and T_b the bulk temperature in the water film. The temperature is considered constant at 0°C across the water film. If the calculated freezing fraction is between 0 and 1, then no changes are made to Q_{wall}. For freezing fractions greater than 1, calculations are done as if all of the water freezes, and for freezing fractions lower than 0, calculations are done as if all of the water is liquid.

In the final case, when all of the water is liquid, temperature variation across the water film thickness is calculated using Eq. (27). Prior to this calculation, thickness of the water film is estimated using the velocity distribution found with Eq. (25). The freezing fraction f is set equal to 0. The surface temperature used for the boundary-layer calculation is no longer the temperature at the water–solid interface but, instead, it is the one at the air–water interface.

The heat at the water–solid interface is given, for the three last cases, by

$$Q_{\text{wall}}=-\dot{m}_{gl}(c_w T_s-L_f)-\dot{H}_{\text{vap}}-\dot{m}_{\text{out}}c_w T_b+\dot{H}_{\text{imp}}+Q_{bl}+\dot{H}_{\text{in}} \qquad (35)$$

The rate of ice accretion $\dot{m}_{gl}$ comes from

$$\dot{m}_{gl}=f\dot{m}_{\text{tot}} \qquad (36)$$

Once the boundary layer is solved and the heat Q_{wall} is found, the temperature distribution in the solid region is calculated. A heat flux Q_{anti}, or a heat transfer coefficient together with a reference temperature, is imposed on the inner side of the airfoil skin. On the external side, when the local freezing fraction is not between 0 and 1, the heat Q_{wall} is imposed. When this is not the case, a surface temperature of 0°C is imposed. The heat Q_{wall} is then estimated in these regions from the temperature distribution in the solid.

With the new surface temperature distribution and, possibly, the new heat Q_{wall}, the boundary-layer equations are solved again before a new temperature distribution in the solid region is sought. The iterative process continues until the total energy leaving the metal skin equals the total energy entering the metal skin.

Because of the temperature and mass concentration variations in the boundary layer, properties of air are not constant. The density changes with temperature and water concentration in the air. The equivalent molecular weight of the mixture is first found with

$$\mathcal{M}=1/[(m_j)_{\text{air}}/\mathcal{M}_{\text{air}}+(m_j)_{\text{vap}}/\mathcal{M}_w] \qquad (37)$$

The molecular weight $\mathcal{M}$ of air and water are, respectively, 28.966 and 18.01 kg/kmol. With $R=8.31434$ Nm/molK, the density of the mixture becomes

$$\rho=\mathcal{M}P_e/RT \qquad (38)$$

Sutherland's law (see Ref. 19) gives the variation of air viscosity with temperature:

$$\mu=1.45^{-6}\frac{(T^{1.5})}{(T+110.3)} \qquad (39)$$

A constant Prandtl number of 0.7 is used to obtain the thermal conductivity. The Schmidt number Sc is a function of the density, through the mass diffusion coefficient for a substance, γ_j:

$$Sc = \mu / \gamma_j \tag{40}$$

$$\gamma_j = \rho D_j \tag{41}$$

where $D_j = 0.25 \times 10^{-4}$ m^2/s is the diffusion coefficient of water in air.

Results and Discussion

Ice Accretion

The numerical results obtained by solving the momentum, energy, and mass diffusion equations for a boundary layer and the two-dimensional conduction equation in the metal skin are first validated using previous numerical results. The code is tested with no heat flux coming from anti-icing device, and ice shapes similar to the ones obtained with CANICE are found.

For all of the cases presented, a sinusoidal distribution is used to discretize the airfoil in 300 panels along the chord. Seven control volumes were used across the metal skin thickness. This mesh density gives a surface temperature distribution independent of the grid.

In Fig. 3, ice shapes accreted after 6 min are plotted for the same atmospheric conditions used for the anti-icing case presented subsequently. Transition point locations are shown in Fig. 3, although their positions are not critical in the case of rime ice accretion presented here. The NACA 0012 airfoil is at an angle of attack of 0 deg, and the velocity is 44.7 m/s. The ambient temperature is -7.6°C. The median volumetric droplet diameter is 20 μm, and the liquid water content is 0.78 g/m^3. The Reynolds number, based on the airfoil chord, is 5.5×10^6 for the calculations.

The collection efficiencies used for the calculations are shown in Fig. 4 as a function of distance from stagnation point on airfoil surface. Two curves are plotted in Fig. 4. The curve ICE is used for icing calculations. The other one, ANTI, is used for anti-icing calculations. The ICE curve is the collection efficiency distribution calculated with CANICE. The ANTI curve comes from Al-Khalil et al.[4] results. Discrepancies between the two curves are discussed by Morency et al.[3]

Ice shape obtained with the finite difference (FD) boundary calculations (CANICE FD) is similar to the one obtained using the classical integral method (CANICE IM) with no conduction in the metal skin. No heat is provided from the anti-icing system, and the metal skin essentially acts to redistribute heat losses in CANICE FD calculations. Temperature contours, from the CANICE FD two-dimensional model of the metal skin, show that temperature is essentially constant across the thickness of the metal skin, except near the end of the icing area. There, heat is removed from the icing area through conduction. This heat is lost by convection in the clean surface area. Ice accretion rates are, thus, higher near the end of the icing area in the CANICE FD case.

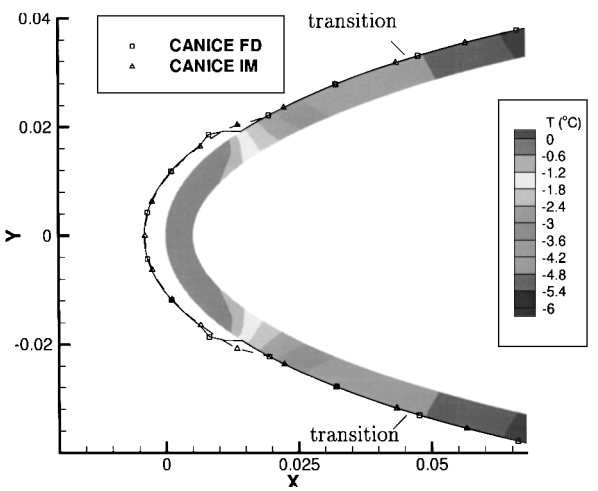

Fig. 3 Ice accretion after 6 min when no anti-icing device is used.

Table 1 Wrap position of the heaters

Heater	Start, cm	End, cm	Power density, kW/m^2
H1	−9.3599	−5.5499	9.920
H2	−5.5499	−3.0099	10.230
H3	−3.0099	−0.4699	32.550
H4	−0.4699	1.4351	46.500
H5	1.4351	3.9751	18.600
H6	3.9751	6.5151	6.975
H7	6,5151	10.3251	10.230

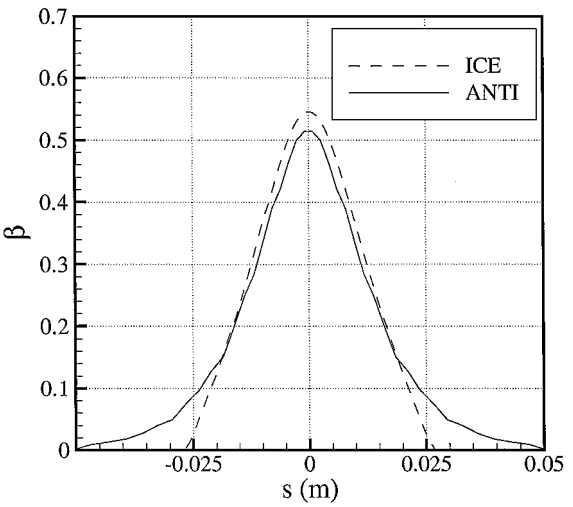

Fig. 4 Collection efficiencies used for the calculations.

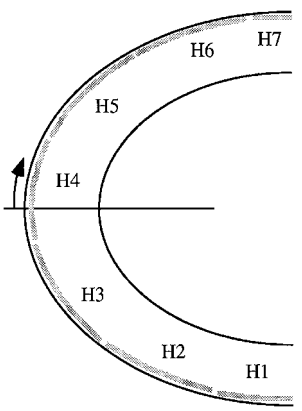

Fig. 5 Heater bands inside the airfoil.

Anti-Icing

The anti-icing code is also validated using the experimental data of Al-Khalil et al.[4] The experimental results were obtained on a NACA 0012, 1.8288-m span and 0.9144-m chord, fitted with an electrothermal ice protection system at the leading edge. The ice protection system consisted of seven heater bands, three on each side of the airfoil and one approximately centered on the leading edge as shown in Fig. 5.

Table 1 lists the wrap coordinates of each of the heaters, together with the power densities used for the present case. Because of the small shift of the heaters toward the airfoil upper part, heating is not symmetric around airfoil leading edge. For example, the heat flux from the H3 heater is almost two times higher than the heat flux from the H5 heater. The electrothermal ice protection system has

Table 2 Material conductivity and thickness from top to bottom of the ice protection system

Layer	Conductivity W/(m · K)	Thickness, cm
1	16.27	0.02
2	0.256	0.028
3	41.02	0.00127
4	0.256	0.028
5	0.294	0.089
6	0.12	0.343

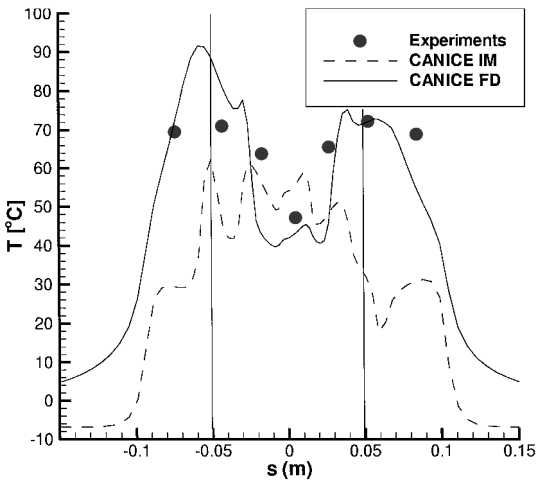

Fig. 6 Comparison of surface temperature distributions.

six layers of different conductivity and thickness, as Table 2 shows. The third layer is the heating element.

With the impinging water mass caught known, the surface temperatures on the airfoil are calculated either by CANICE IM or by CANICE FD. To help in the comparisons, transition from laminar to turbulent boundary layer is imposed at the same location, $s/c = 0.055$, on the airfoil upper part and lower part.

Figure 6 shows the numerical surface temperature distributions estimated with the IM and with the FD method as a function of curvilinear position along surface. Vertical lines are draw at transition point locations. Because of asymmetric heating, surface temperatures are higher on the lower part of the airfoil. The experimental results of Al-Khalil et al.[4] are also shown. From Fig. 6, it is clear that the FD method gives a better approximation of the experimental temperatures. This is particularly true after the transition points, where the smooth transition model used with the FD method avoids an abrupt change in surface temperature.

In the case of surface temperatures obtained with CANICE FD, inertia effects in the heated boundary layer retard the cooling of the surface in some areas. This is visible past the heated region, near $s = 0.1$ m, where surface temperature drops slowly instead of going down abruptly, as in the case of CANICE IM results. There is more than 10°C of difference in surface temperature past $s = 0.15$ m. Farther downstream, the two calculated surface temperatures become almost equal.

Looking at the friction coefficient distributions in Fig. 7 gives an idea of the water evaporation effects on the boundary-layer velocity profile. For this particular case, with a small mass rate of water caught and, thus, a small mass of water evaporated, no effects are clearly visible on the friction coefficient distribution from CANICE FD. CANICE IM calculations do not take into account the variation of air properties nor the blowing effect caused by water evaporation. CANICE FD and IM results look the same, except near $s = 0.05$ m, where the effect of smooth transition from laminar to turbulent boundary layer is visible.

The mass losses due to evaporation are compared in Fig. 8 for the two methods. Because surface temperatures are not the same, evaporation rates in the two cases are clearly different. The evaporated water mass rises when surface temperature rises and falls when surface temperature falls. Evaporation rates are greater in CANICE FD calculations. Because of the water high latent heat of evaporation, the difference in the evaporated water mass near the stagnation point is enough to cause a change of more than 10°C in the calculated surface temperature.

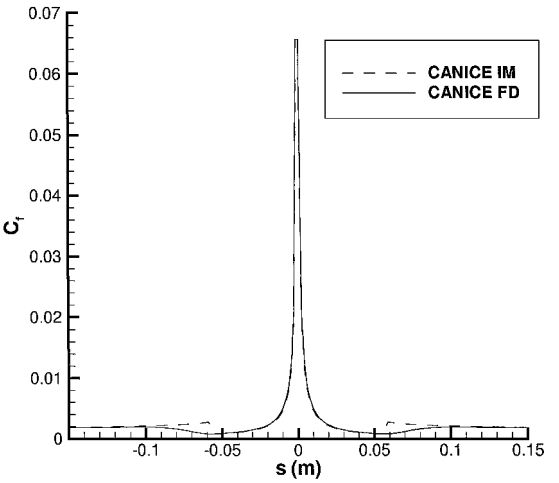

Fig. 7 Comparison of friction coefficients.

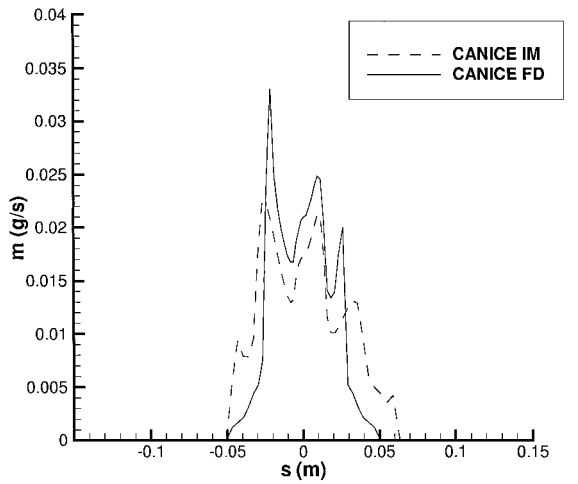

Fig. 8 Comparison of mass loss to evaporation.

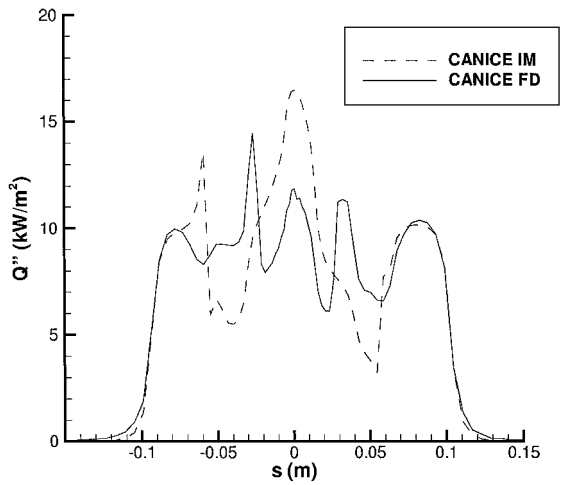

Fig. 9 Comparison of heat loss to convection.

Heat losses due to convection are presented in Fig. 9 for CANICE IM and CANICE FD calculations. Because no heat is provided past

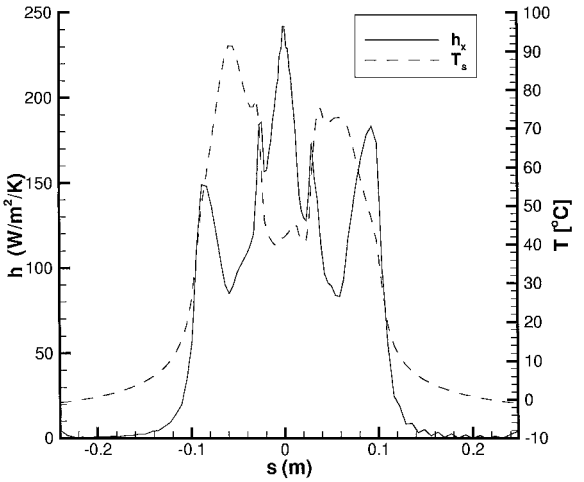

Fig. 10 Surface temperatures and heat transfer coefficients for FD calculations.

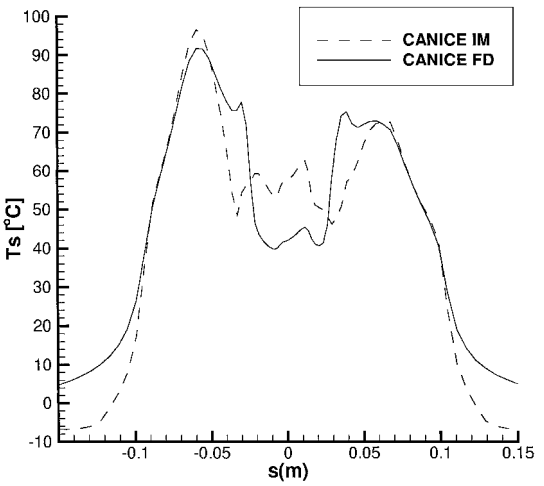

Fig. 11 Surface temperatures obtained with the same heat transfer coefficients.

$s = 0.1$ m, heat lost to convection falls quickly near 0, although this does not mean that the heat transfer coefficients are 0. Far from the heated and the wet area, the metal skin is in equilibrium with the external airstream. By definition,

$$Q_{bl} = h_x(T_s - T_{\text{ref}}) \tag{42}$$

and if $T_s = T_{\text{ref}}$, then $Q_{bl} = 0$ and the heat transfer coefficient h_x is indefinite.

Losses to convection in the stagnation point area are greater in CANICE IM calculations because surface temperatures are greater. The evaporation rates, lower in CANICE IM than in CANICE FD, cause the higher surface temperatures.

In Fig. 10, surface temperatures together with heat transfer coefficients are plotted for CANICE FD calculations. Variations of the temperature with the heat transfer coefficient are clearly visible. In addition, a sharp rise occurs in the heat transfer coefficient when the temperature increases near $s = 0.04$ m. This kind of rise is not modeled with the hypothesis of constant surface temperature used in the IM.

Finally, to see the effect of the heat transfer coefficient values used, the heat transfer coefficients calculated by the FD method have been employed in CANICE IM calculations. Surface temperature distributions in Fig. 11 show that in the impinging water area, temperatures calculated by CANICE IM are higher than those calculated by CANICE FD. For the same heat transfer coefficients, evaporation rates are lower with the IM calculations. When there is no water on the airfoil, agreement between surface temperatures is better. Discrepancies after $s = 0.1$ m are caused by the heat transfer coefficients from CANICE FD being indefinite. Thus, outside of the heating area, heat transfer coefficients from the IM must be used in CANICE IM.

Conclusions

A mathematical model to solve the boundary layer around an airfoil with heat and mass transfer has been presented. This mathematical model has been implemented successfully in the CANICE code. The modified version of CANICE is able to predict heat and mass transfer, surface temperature, and ice accretion for icing or anti-icing cases.

A two-dimensional model of the metal skin has also been implemented in CANICE. Numerical results for several cases showed that two-dimensional effects are not always negligible at the end of the wetted surface. However, when an ice protection system uses an electrothermal device, instead of a hot air anti-icing device, two-dimensional effects are small because the heating device is close to the surface.

The heat transfer coefficients found with the integral boundary-layer method are not in perfect agreement with the ones found with the FD method. Results show that heat transfer coefficients from the FD method are closer to the experimental ones. Even when the heat transfer coefficients from the FD calculations are used, the evaporation rates found by analogy with heat transfer are too low for the case studied here. The relation used to calculate evaporation rates by analogy from heat transfer coefficients should be verified.

Finally, the FD method used to solve the boundary layer offers flexibility in the simulation of the laminar–turbulent transition region. The smooth variation of the heat transfer coefficient makes the choice of the transition point less critical. A roughness model must be added to take into account the state of the surface when ice accretion occurs, for example, when the anti-icing device does not provide enough heat.

Acknowledgments

The authors would like to acknowledge the support of Natural Sciences and Engineering Research Council of Canada through a cooperative research and development grant with Bombardier Aerospace. The first author would also like to thank the Fonds pour la Formation de Chercheurs et de l'Aide à la Recherche for financial support.

References

[1]Thomas, S. K., Cassoni, R. P., and MacArthur, C. D., "Aircraft Anti-Icing and Deicing Techniques and Modeling," *Journal of Aircraft*, Vol. 33, No. 5, 1996, pp. 841–854.

[2]Al-Khalil, K. M., Ferguson, T. W., and Phillips, D. M., "A Hybrid Anti-Icing Ice Protection System," AIAA Paper 97-0302, Jan. 1997.

[3]Morency, F., Brahimi, M. T., Tezok, F., and Paraschivoiu, I., "Hot Air Anti-Icing System Modelization in the Ice Prediction Code CANICE," AIAA Paper 98-0192, Jan. 1998.

[4]Al-Khalil, K. M., Horvath, C., Miller, D. R., and Wright, W. B., "Validation of NASA Thermal Ice Protection Computer Codes. III—The Validation of ANTICE," AIAA Paper 97-0051, Jan. 1997.

[5]Al-Khalil, K. M., "Numerical Simulation of an Aircraft Anti-Icing System Incorporating a Rivulet Model for the Runback Water," Ph.D. Thesis, Engineering Science, Univ. of Toledo, Toledo, OH, June 1991.

[6]Al-Khalil, K. M., and Potapczuk, M. G., "Numerical Modeling of Anti-Icing Systems and Numerical Comparison to Test Results on a NACA 0012 Airfoil," AIAA Paper 93-0170, Jan. 1993.

[7]MacArthur, C. D., "Numerical Simulation of Airfoil Ice Accretion," AIAA Paper 83-0112, Jan. 1983.

[8]Brunet, L., "Conception et Discussion d'un Modèle de Formation du Givre sur des Obstacles Variés," FR ISSN 0078-3781, ONERA, Chatillon, France, 1986.

[9]Tran, P., Brahimi, M., and Paraschivoiu, I., "Ice Accretion on Aircraft Wings with Thermodynamic Effect," AIAA Paper 94-0605, Jan. 1994.

[10]Makkonen, L., "Heat Transfer and Icing of a Rough Cylinder," *Cold Region Science and Technology*, Vol. 10, 1985, pp. 105–116.

[11]Henry, R., "Development of an Electrothermal De-Icing/Anti-Icing

Model," AIAA Paper 92-0526, Jan. 1992.

[12]Brahimi, M. T., Tran, P., Chocron, D., Tezok, F., and Paraschivoiu, I., "Effect of Supercooled Large Droplets on Ice Accretion Characteristics," AIAA Paper 97-0306, Jan. 1997.

[13]Kays, W. M., and Crawford, M. E., *Convective Heat and Mass Transfer*, 3rd ed., McGraw–Hill, New York, 1993, Chaps. 10, 13, 20, and 21.

[14]Cebeci, T., and Bradshaw, P., *Physical and Computational Aspects of Convective Heat Transfer*, Springer–Verlag, New York, 1984.

[15]Meyer, C. A., *ASME Steam Tables*, 6th ed., American Society of Mechanical Engineers, New York, 1993, Appendix 1, pp. 20–40.

[16]Moran, J., *An Introduction to Theoretical and Computational Aerodynamics*, Wiley, New York, 1984, Chaps. 7, 8.

[17]Press, W. H., Teukolsky, S. H., Vetterling, W. T., and Flannery, B., *Numerical Recipes in FORTRAN (The Art of Scientific Computing)*, 2nd ed., Cambridge Univ. Press, New York, 1992, Chap. 16.

[18]Patankar, S. V., *Numerical Heat Transfer and Fluid Flow*, Series in Computational Methods in Mechanics and Thermal Sciences, Taylor and Francis, Washington, DC, 1980, Chaps. 2 and 3.

[19]White, F. M., *Fluid Mechanics*, 3rd ed., McGraw–Hill, New York, 1994, Chap. 6.